Interaction of small mobile stacking fault tetrahedra with free surfaces, dislocations, and interfaces in Cu and Cu-Nb

Enrique Martínez,[1,*] Blas P. Uberuaga,[1] and Irene J. Beyerlein[2]
[1]*Material Science and Technology Division, MST-8, Los Alamos National Laboratory, Los Alamos, New Mexico 87545, USA*
[2]*Theoretical Division, T-3, Los Alamos National Laboratory, Los Alamos, New Mexico 87545, USA*
(Received 2 November 2015; published 4 February 2016)

The presence of stacking fault tetrahedra (SFTs) in face-centered-cubic metals substantially modifies the material response to external loading. These defects are extremely stable with increasing energetic stability as they grow in size. At the sizes visible within a transmission electron microscope, they appear nearly immobile. We have recently shown that these defects might indeed migrate, with defective SFTs exhibiting particularly high mobilities. In this paper, using molecular dynamics, we show how mobile SFTs interact with various types of extended defects, including free surfaces, dislocations, and interfaces in Cu and Cu-Nb systems. We observe a direct relation between the energetics of a single vacancy interacting with each external defect and the propensity for the SFT to be absorbed. Finally, using mesoscale modeling, we show how the fact that SFTs can migrate influences the system evolution and potentially important observables of interest such as the void denuded zones around defect sinks.

DOI: 10.1103/PhysRevB.93.054105

I. INTRODUCTION

Stacking fault tetrahedra (SFTs) present a significant source of hardening in structural face-centered-cubic (fcc) metals [1,2] as they interact with dislocations and hinder their motion [3–10]. SFTs might be produced by a variety of processes such as heavy plastic deformation [11], quenching from temperatures close to the melting point [12,13] or via irradiation [14–17]. From a dislocation viewpoint, SFTs consist of a set of stair-rod dislocations at the edges of a tetrahedron. These stair rods are predicted to be immobile [18], and therefore the SFTs are commonly thought to be an immobile defect. Even for the smallest of vacancy clusters, containing as few as six vacancies, molecular dynamics (MD) simulations predict that the SFT structure is the most stable configuration. Thus, with the exception of vacancy clusters containing less than six vacancies [19], large vacancy clusters that universally adopt the SFT structure have been assumed to be essentially immobile.

We recently showed that, despite their large stability, SFTs are indeed mobile defects, even faster than single vacancies for small sizes ($\sim$12 vacancies) [20]. We observed that defective SFTs (with a number of vacancies different from a perfect triangular Frank loop) can migrate with a diffusion coefficient orders of magnitude larger than perfect SFTs. Migration of SFTs brings up the possibility of the direct interaction of SFTs with microstructural defects such as free surfaces, dislocations or grain boundaries, and interfaces. That is, in contrast to earlier studies in which mobile defects such as dislocations were examined in the presence of immobile SFTs, our recent results indicate that the SFTs themselves are mobile and should not be regarded only as obstacles.

This work focuses on the analysis of these interactions and their possible outcomes. To this end, MD simulations have been performed on systems containing different types of extended defects. We study the interaction of SFTs with {110}, {111}, and {112} free surfaces in single-phase Cu, which are of interest in irradiated nanofoams as they are the dominant sinks in those types of materials [21,22]. We also analyze the interaction of SFTs with edge and screw dislocations in single-phase Cu, which dissociate into Shockley partials bounding a stacking fault ribbon. We study homophase interfaces in single-phase Cu and heterophase interfaces in Cu-Nb nanocomposites as these types of interfaces have been examined for their potential utility as sinks for radiation-induced defects [23,24]. More specifically, in single-phase Cu we investigate the reaction of SFTs with a $\Sigma 3$ twin, $\Sigma 5$ twist, asymmetric $\Sigma 11$ tilt, and 2° {111} twist and 4° {100} twist boundaries, which represent different densities and patterns of misfit structures and dissimilar interactions with monovacancies. In the Cu-Nb alloy we study the interaction of SFTs with Kurdjumov-Sachs (KS) heterophase interfaces with orientations similar to those synthesized experimentally by physical vapor deposition (PVD) and accumulative roll bonding (ARB) techniques [25]. Finally, having established that there are indeed strong interactions between mobile SFTs and these various microstructural features, we study the implications of this interaction on a macroscopic observable using an object kinetic Monte Carlo approach, finding substantial differences in the predicted microstructure as a consequence of the high SFT mobility. In particular, we find that the extent of void denuded zones is sensitive to the mobility of SFTs, and that the predicted response to irradiation requires an accounting of the mobilities of these ubiquitous defects.

II. METHODOLOGY

Table I summarizes the various simulations performed, providing the dimensions, number of atoms, and sizes of the SFTs in the MD samples used in this work. The orientation relationships that describe the different interfaces can be found in Refs. [25,26]. The MD code LAMMPS [27] is used with the Mishin *et al.* embedded atom method (EAM) potential for Cu [28] and the Zhang *et al.* EAM potential for Cu-Nb [29].

*enriquem@lanl.gov

 ©2016 American Physical Society

TABLE I. Dimensions, number of atoms (before introduction of SFTs), and SFT sizes of the MD samples for the various extended defect configurations examined in this study.

Boundary	Dimensions (nm)	Atoms	SFT
{111} Surface	3.8 × 3.1 × 3.5	3,456	12V/18V
{110} Surface	id	id	id
{112} Surface	id	id	id
Edge dislocation	8.8 × 20.4 × 18.7	286,200	12V
Screw dislocation	26.7 × 20.5 × 13.2	691,200	12V
AΣ11 tilt	8.9 × 7.2 × 16.9	88,704	12V/18V
4°{100} twist	12.4 × 12.4 × 25.1	314,704	12V/18V
Σ5 twist	5.8 × 5.8 × 7.4	20,000	12V/18V
2°{111} twist	15.5 × 8.9 × 22.1	252,210	12V
SΣ11 tilt	8.5 × 9.2 × 14.4	95,040	12V
Σ3	6.3 × 5.2 × 17.7	47,040	12V/18V
PVD KS	15.5 × 15.5 × 15.1	249,696	12V/18V
ARB KS	9.8 × 8.1 × 7.6	41,172	12V

The calculations are performed in the NPT ensemble with fully periodic boundary conditions, Berendsen barostat at 0 MPa, and Langevin thermostat at 700 K, which alleviates the MD time-constraint problem as the defect mobilities at this temperature are significant [20]. SFTs are created by removing a triangular region of atoms as far as possible from the surface, dislocation, or interface examined, with extra sites removed to form a defective SFT (and thus increase their mobility). Upon relaxation with a conjugate gradient method, the SFT is formed. For some of the extended defect structures, two different SFT sizes are tested in this work, 12 and 18 vacancies (12V and 18V respectively), that are characterized by high mobilities [20]. It is worth remarking that the final configurations observed in this study are constrained to the MD time-scale limitation and further reactions might take place on a longer time scale that we are not able to capture here. The software OVITO [30] was used for visualization and a common neighbor analysis to identify the crystalline structure of the atoms [31].

III. RESULTS

A. Free surfaces

Three free surfaces have been studied, the {110}, {111}, and {112}. In all three cases we observed, as the SFT migrated toward the surface, the full absorption of the SFT, as shown in Fig. 1, where the structures at the first interaction and after the subsequent absorption are presented. The figure shows the results for the 12V SFT, although the process is similar for the 18V SFT, with full removal of the SFT. Despite the fact that the SFT is finally fully absorbed, it is worth noting that there is an energetic barrier for the vacancy cluster to reach the sink. We observe parallel diffusion of the SFT with respect to the surface. That is, for much of the simulation, the SFT's migration is confined to dimensions perpendicular to the surface normal. In this respect, not all the surfaces act exactly the same way, with the {112} surface presenting the lowest barrier, followed by the {110} and lastly the {111}, which has the highest barrier. These results have implications in the field of nanoporous materials under irradiation, where the formation of SFTs has been observed experimentally. The possibility of annihilation of SFTs at surfaces would lead to a reduction of defect (dislocation obstacles) concentrations and therefore a decrease in hardening.

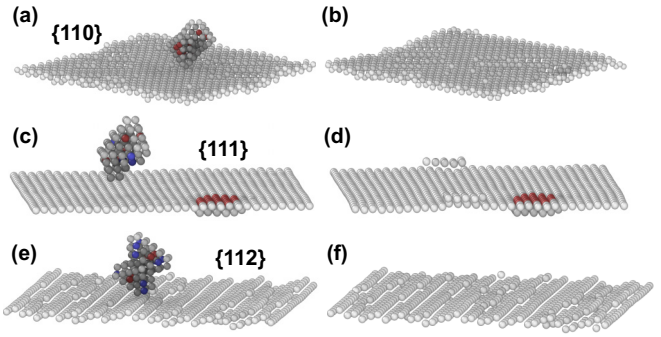

FIG. 1. 12V-SFT interacting with (a) and (b) a {110}; (c) and (d) a {111}; and (e) and (f) a {112} free surfaces in single-phase Cu. Atoms are colored according to their structure (as determined by a common neighbor analysis): hcp as red, bcc as blue, and unknown structure as white; fcc atoms are not shown for clarity. In panels (a), (c), and (e), the configuration as the SFT first directly interacts with the surface is provided, while the configuration after full absorption of the SFT by each surface is provided in panels (b), (d), and (f). The perspective is from inside the material, viewing the surface from within.

B. Single dislocations

Concerning single dislocations, much work has been devoted to the study of the interaction of mobile dislocations with sessile SFTs under applied stress [2,7–10,32–40]. In this work we focus on the interaction, at elevated temperature, between defective mobile SFTs and edge and screw dislocations, which are dissociated into Shockley partials bounding a stacking fault ribbon. At this temperature, both dislocations and SFTs are mobile. Dislocations are in the phonon-drag regime, substantially above the Peierls barrier, with their movement constrained to the glide plane. The SFTs move in a thermally activated fashion, following a three-dimensional (3D) random walk (as opposed to the constrained pseudo-two-dimensional [2D] behavior seen near the interfaces). Figure 2 shows the resulting configuration for the interaction on a 12V SFT with the dislocations (the 18V-SFT-dislocation interaction results in a similar structure). In both cases, the interaction is attractive. In the case of the edge dislocation, the vacancies of the SFT are absorbed by one of the Shockley partials,

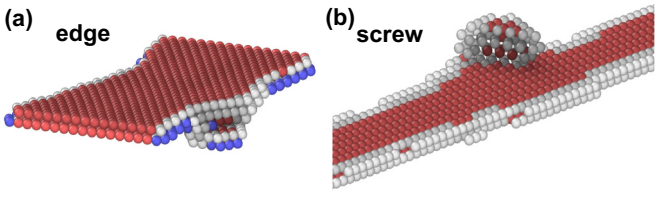

FIG. 2. Resulting configuration after the interaction of a 12V SFT with (a) an edge dislocation and (b) a screw dislocation in single-phase Cu. Dislocations are split into Shockley partials bounding a stacking fault ribbon. The color coding is the same as in Fig. 1.

resulting in a localized jog at the partial dislocation; i.e., the jog does not extend through the stacking fault to reach the second Shockley partial. We do not observe pinning of the dislocation after the climbing process, and the dislocation keeps moving thermally (without any applied stress) as prior to the reaction. For the screw, the vacancies within the SFT were not absorbed by the Shockley partial, although the SFT is attached to the dislocation; again no pinning was observed and the thermal behavior of the dislocation remained unchanged after the interaction, with the resulting extended defect (dislocation+SFT) migrating as a whole.

C. Homophase interfaces

Homophase interfaces, i.e., grain boundaries, have been extensively studied in the context of radiation damage for their potential use as sinks to mitigate radiation damage accumulation [23,24,41]. An important factor determining the sink efficiency of these interfaces is the interaction of defects with individual interfacial planes. Here we analyze a subset of boundaries and their interaction with mobile SFTs to determine how these more complicated extended defects interact with the boundaries and thus contribute to their sink properties. Figure 3 shows the interaction of $12V$-SFT and $18V$-SFT with an asymmetric $\Sigma 11$ tilt grain boundary. This interface [26] is characterized by a set of Shockley partials ($\mathbf{b} = \frac{1}{2}\{112\}$) extending out of one side of the boundary, as shown in the figure. Figures 3(a) and 3(c) present the initial interaction between the $12V$- and $18V$-SFTs and the interface, respectively. For the $12V$-SFT it can be readily seen that the SFT attracts one of the Shockley partials, pulling it out of the interface so that it reacts with one of the stair rods ($\mathbf{b} = \frac{1}{6}\{110\}$) at the edge of the SFT. For the $18V$-SFT, the first reaction takes place between a Shockley partial at the boundary and one apex of the distorted SFT, and because of core overlap, cannot be rationalized in terms of dislocation reactions. The final configurations of the system after absorption of the SFT into the boundary are shown in Figs. 3(b) and 3(d), where little to none of the original SFT structure can be distinguished. The final configuration will be further analyzed and discussed in Sec. IV.

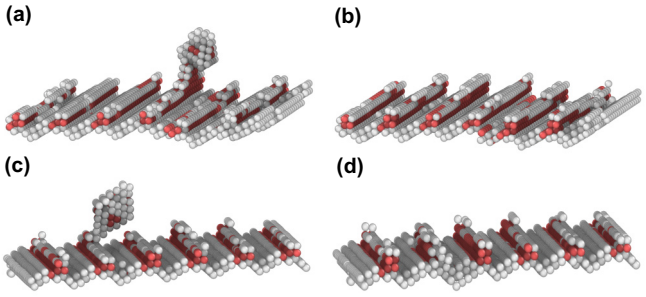

FIG. 3. (a) and (b) $12V$-SFT and (c) and (d) $18V$-SFT interacting with an asymmetric $\Sigma 11$ tilt grain boundary in Cu. Panels (a) and (c) show the initial interaction of the SFT with the boundary while panels (b) and (d) display the final configuration, after the SFT has been absorbed by the boundary. The color coding is the same as in Fig. 1.

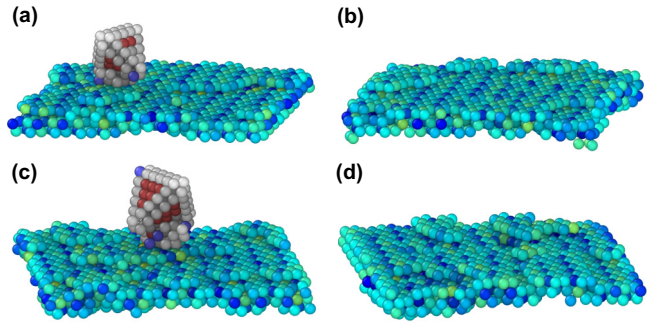

FIG. 4. (a) and (b) $12V$-SFT and (c) and (d) $18V$-SFT interacting with a $\Sigma 5$ twist grain boundary in Cu. Panels (a) and (c) show the initial interaction while panels (b) and (d) display the final configuration after absorption. The interface is colored according to σ_{xx} on each atom calculated with the virial theorem while the SFT is colored according to the atomic structure (hcp and unknown coordination as red and white, respectively).

For the case of the $\Sigma 5$ twist grain boundary, shown in Fig. 4, both the $12V$-SFT and $18V$-SFT are absorbed at the interface leaving no debris behind, similar to what was observed for the asymmetric $\Sigma 11$ tilt boundary. This interface cannot be characterized in terms of misfit dislocations since the misfit dislocation cores overlap significantly and individual discrete dislocations cannot be distinguished. However, this type of interface presents a large attraction for vacancies since it presents a very flexible atomic structure.

We also studied the interaction of a $12V$-SFT and a $18V$-SFT with a low-angle 4° $\{100\}$ twist boundary in Cu (see Fig. 5). In contrast to the $\Sigma 5$ twist, the structure of this low-angle twist boundary is characterized by a regular square array of misfit dislocations with $\langle 110\rangle$ Burgers vector that dissociate in the $\{111\}$ planes into Shockley partials, forming constrictions between the misfit dislocation intersections (MDIs) [42]. We have shown previously (see Ref. [42]) that the preferential sites for vacancies lie at the MDIs, with the Shockley partials also being favorable positions. As the SFT reaches this interface, it reacts with one Shockley, becomes

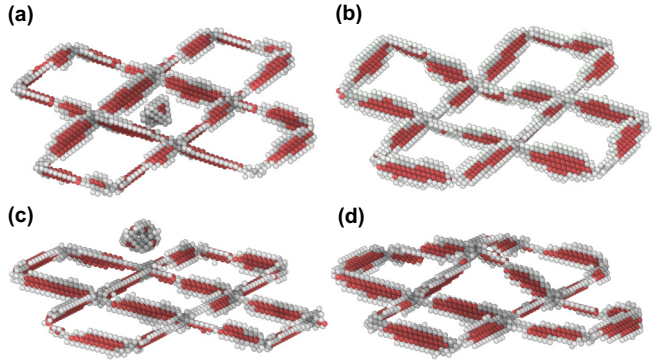

FIG. 5. (a) and (b) $12V$-SFT and (c) and (d) $18V$-SFT interacting with a 4° $\{100\}$ twist boundary in Cu. Panels (a) and (c) show the initial interaction of the SFT with the boundary while panels (b) and (d) show the final configuration after absorption. The color coding is the same as in Fig. 1.

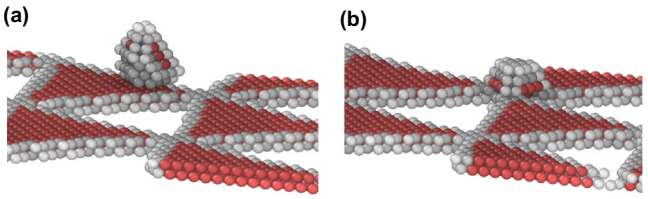

FIG. 6. Interaction of a $12V$-SFT with a 2° {111} twist boundary in Cu. (a) Initial interaction; (b) final configuration. The color coding is the same as in Fig. 1.

absorbed, and subsequently migrates (along the dislocation core) to an MDI. In both cases, $12V$ and $18V$, we observe the subsequent climbing of the MDI due to the absorption of vacancies associated with the SFTs.

The interaction of a $12V$-SFT and a 2° {111} twist boundary is presented in Fig. 6. This interface, with a {111} habit plane, is formed by a set of Shockley partials bounding stacking fault regions and fully coherent regions. The first reaction of the SFT with this boundary, as the SFT migrates through the sample, takes place between a Shockley partial and a stair rod from the SFT [Fig. 6(a)]. As presented in a previous study [43], the formation energy of a single vacancy is lowest at the MDIs, as it was for the 4° {100} twist boundary. We note that once the reaction takes place at the dislocation, the defect migrates until it reaches one MDI, where it remains for the rest of the calculation, a consequence of the low vacancy formation energy there, a point we will elaborate on below. In contrast to the previous boundaries studied, in this case the SFT is not fully absorbed but a remnant is left at the MDI, where the stair-rod dislocations forming the initial SFT are still distinguishable. Thus, in this case, the SFT, while still existing as an identifiable entity, is trapped at the interface, which essentially retains its structure. It is interesting that at both low-angle twist boundaries, the SFT migrates along the dislocations until it reaches an MDI, but in the cases of the isolated dislocations, the dislocation-SFT complex as a whole migrated. This is possibly the consequence of the relatively high mobility of the dislocation when it is isolated as compared to when it is part of a network of dislocations.

Figure 7 illustrates the interaction between the symmetric $\Sigma 11$ tilt boundary and a $12V$-SFT. As for the $\Sigma 5$ twist, the interface cannot be described in terms of misfit dislocations. The atoms belonging to the interface are characterized in terms of their atomic structure and those that do not have an fcc coordination are highlighted. The interaction is attractive, the SFT attaches to the interface but is not fully absorbed, and the structure of the SFT remains distinct from the interface.

Finally, we analyzed the interaction of both a $12V$-SFT and a $18V$-SFT with a $\Sigma 3$ twin boundary, possibly the simplest type of boundary that can be formed in fcc materials. In this

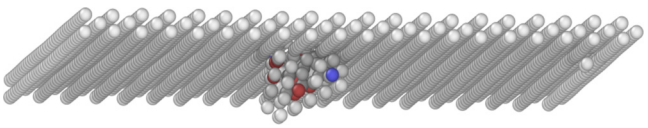

FIG. 7. Final configuration of a $12V$-SFT interacting with a $\Sigma 11$ tilt boundary in Cu. The color coding is the same as in Fig. 4.

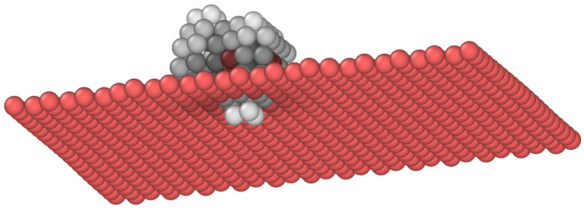

FIG. 8. $12V$-SFT interacting with a $\Sigma 3$ twin boundary in Cu. The color coding is the same as in Fig. 1.

boundary, no misfit dislocations are present and the atomic distortion is minimal, which leads to an essentially negligible interface-vacancy interaction. Figure 8 shows the interaction of the $12V$-SFT with the interface. For both SFT sizes we observe that, while the boundary does not absorb the SFT, it does act as a barrier for SFT migration, confining the defects to one side of the boundary. The figure displays the closest the SFT comes to penetrating the interface. The different orientation of the grains on each side of the boundary prevents the crossing of the SFT, while the minimal ability of this boundary to attract single vacancies hinders absorption. Thus, in contrast to the other boundaries, this interface does not act as a sink for SFTs but rather an obstacle.

D. Heterophase interfaces

Figure 9 shows the interaction of a $12V$-SFT and a $18V$-SFT with a PVD KS heterophase interface. The system contains two heterophase interfaces with a Kurdjumov-Sachs (KS) orientation relationship such that the interface plane is $\{111\}$fcc $\parallel \{110\}$bcc, and within the interface plane, $\langle 110\rangle$fcc $||\langle 111\rangle$bcc. Each layer has a thickness of 7.5 nm. The orientation in the Cu layer is given by $x = [11\bar{2}]$, $y = [\bar{1}10]$, and $z = [111]$. This interface is characterized by two sets of

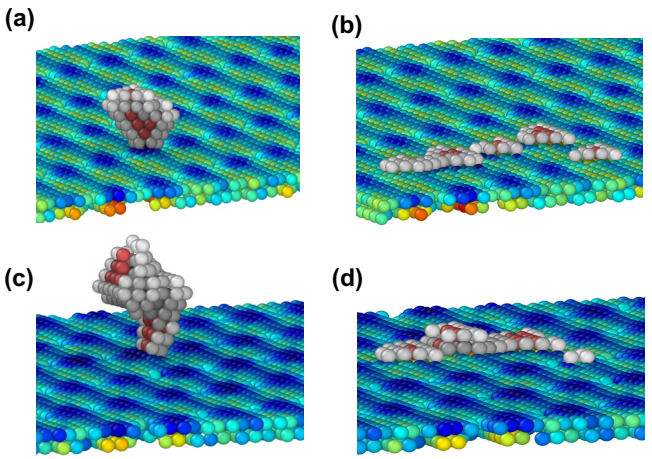

FIG. 9. (a) and (b) Interaction of a 12V-SFT with a KS1 hetero-interface in Cu-Nb. Panel (a) shows the first reaction and panel (b) shows the final interface configuration. (c) and (d) Interaction of a 18V-SFT with a KS1 hetero-interface: Panel (c) shows the first reaction and panel (d) shows the final configuration. The color coding is the same as in Fig. 4. The dark blue regions correspond to the locations of the MDIs within the interface. In this perspective, the view is from inside Cu, looking down on the interfacial plane.

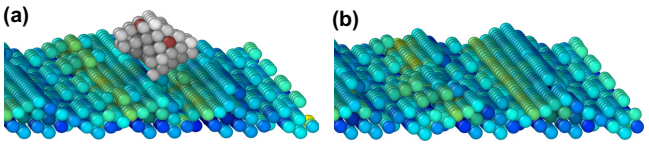

FIG. 10. $12V$-SFT interaction with an ARB KS hetero-interface in Cu-Nb. Panel (a) shows the initial interaction and panel (b) illustrates the final interface configuration after the SFT has been absorbed. The color coding is the same as in Fig. 4.

misfit dislocations, which confer remarkable properties to the system both under irradiation and deformation [44–46]. MDIs are preferential sites for vacancy accumulation, as the vacancy formation energy is lower at those sites [44,47]. Figures 9(a) and 9(c) highlight the first contact between the migrating SFT and the interface for a $12V$-SFT and a $18V$-SFT respectively. We observe that the SFT reacts with the interface close to one MDI (dark blue regions). Both SFTs are attracted to the interface, ultimately becoming absorbed. Figures 9(b) and 9(d) present the structure after absorption as obtained by the MD simulations, displaying certain remnants of the SFT interspersed within the interface. Although the debris seems to be fairly stable (on MD time scales), the SFT structure becomes totally disrupted, which seems to indicate that the interface behaves as a sink for the SFTs.

We have also studied the interaction of a $12V$-SFT with an ARB KS interface (Fig. 10). The system was built with an orientation relationship given by {112}fcc ∥ {112}bcc and within the interface plane, ⟨110⟩fcc ∥ ⟨111⟩bcc, which is a KS interface with a {112} habit plane. The interface in this case is also characterized in terms of dislocations. While their structure is more convoluted than for the PVD KS interface, the Burgers vectors can be obtained following a disregistry analysis [25]. Upon reaching the interface, the SFT reacts with the interface and it is completely absorbed, with no debris observed in the final configuration [Fig. 10(b)].

IV. DISCUSSION

The MD results reveal that the interaction of SFTs with various microstructural defects varies as a function of structure of those extended defects. In some cases, SFTs are completely absorbed. In others, they are only partially absorbed. Finally, in the case of the Σ3 twin, the SFT is not absorbed at all. To understand the origins of these differences in behavior, we analyze the fundamental properties associated with each extended defect.

The interaction energy of a single vacancy with the various surfaces, dislocations, and interfaces examined is shown in Table II. We have also calculated the Voronoi volume of the atoms at the interface. We have defined the atoms at the interface as those that do not belong to the bulk, being neither bcc nor fcc structures according to a common neighbor analysis [30] (note that the definition of the Voronoi volume breaks down for the surface atoms). The goal of this analysis is to identify correlations between the basic properties of the extended defect (free surfaces, dislocations, and interfaces) and the absorption mechanism of SFTs at each sink. Further, in the case of single vacancies, we have previously found

TABLE II. Properties of extended defects as they relate to the interaction with SFTs: vacancy interaction energy with different extended defects in single-phase Cu and Cu-Nb, and maximum (Ω_{max}) and minimum (Ω_{min}) atomic volume at the interface. The SFT column indicates if in the final configuration the SFT has been fully absorbed (FA), partially absorbed (PA), or not absorbed (NA).

Boundary	E^{Int}_{V-B} (eV)	Ω_{max} (Å^3)	Ω_{min}(Å^3)	SFT
{111} Surface	−0.51			FA
{110} Surface	−0.98			FA
{112} Surface	−1.00			FA
Edge dislocation	−0.25	12.27	11.54	PA
Screw dislocation	−0.22	12.18	11.67	PA
AΣ11 tilt	−0.54	13.35	11.36	FA
{100} twist	−0.53	12.28	11.61	FA
Σ5 twist	−0.5	13.42	11.65	FA
{111} twist	−0.4	12.41	11.7	PA
SΣ11 tilt	−0.2	12.55	11.75	PA
Σ3	0	11.81	11.81	NA
PVD KS	−0.69	19.55	11.20	FA
ARB KS	−0.81	19.02	11.13	FA

correlations between the formation energy and Voronoi volume at grain boundaries [48]. The interaction energy is defined as

$$E^{int}_{V-B} = E^{defect}_{V} - E^{bulk}_{V} \quad (1)$$

where E^{defect}_{V} is the energy of the system with the vacancy at the surface, dislocation or interface and E^{bulk}_{V} is the energy of the system with the vacancy far from those extended defects, all calculated at zero pressure. With this definition, as the value is more negative, the attraction is greater. For each extended defect structure, a set of representative atoms near and at the structure was selected and each atom was removed (i.e., replaced by a vacancy), one atom at a time, and each time the energy of the relaxed system was calculated. In Table II, we report the energy of the lowest energy structure found, compared to the bulk value, which was obtained by removing an atom located as far as possible from the interface in our simulation cells and relaxing the system.

As reported in Table II, for the free surfaces, the attractive interaction is high, which leads to a full absorption of the SFTs. In the case of dissociated dislocations the interaction energy is about −0.25 eV, which leads to an attraction between the SFT and the dislocation cores with partial absorption. For the homophase interfaces, as the interaction is more attractive, the propensity is greater for absorption of the SFT. For values between −0.54 and −0.5 eV, corresponding to the asymmetric Σ11 tilt, {100} twist, and Σ5 twist, the SFT was fully absorbed. For weaker interaction energies, ranging from −0.4 to −0.2 eV ({111} twist and symmetric Σ11 tilt), the SFT was partially absorbed. For the case where no interaction energy exists (Σ3 boundary), the SFT remained fully structured when interacting with the interface with no appreciable interaction. However, it remains constrained within the layers between the boundaries (as we have periodic boundary conditions in all directions); i.e., the probability for the SFT to cross the interface is low, likely due to the change in crystal orientation. Thus, in this case, because the interaction is low, the boundary cannot absorb the

SFT, but neither can the SFT cross the boundary, which acts as an obstacle. This observation is compatible with experimental evidences [49,50] that show that smaller twin spacing leads to fewer SFTs, since the probability of recombination of interstitials and SFTs increases. However, we did not observe full absorption of SFTs in the coherent twist boundary, as reported in the experiments. One possible explanation is the difference in time scales, with experiments going over 5 s. A second explanation is the possibility of defected interfaces, with the presence of interstitial loops that we do not consider here.

These results indicate a direct correlation between the single-vacancy interaction energy and the propensity for the extended defect to absorb SFTs. We are aware that the set of data presented in this work is not exhaustive and this analysis might change if more interface structures were considered. However, this correlation makes physical sense. If the single vacancy is strongly attracted to the extended defect, then it can easily absorb vacancies, which are the defects that comprise the SFT. In contrast, if the extended defect cannot absorb even single vacancies, it will not be able to absorb the large collection of vacancies that is the SFT. This analysis neglects

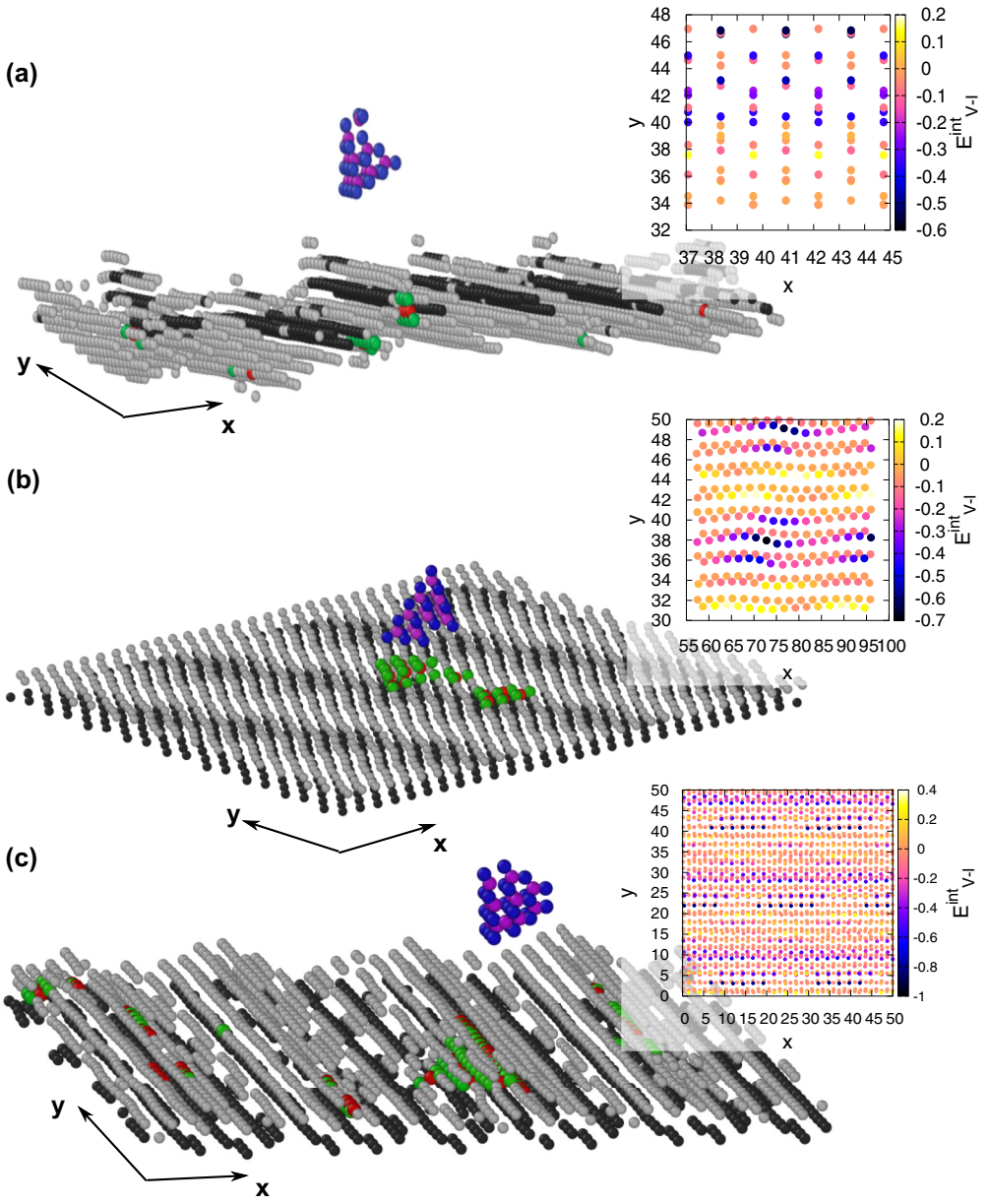

FIG. 11. Analysis of the atomic displacement before and after the interaction of a 12V-SFT with the (a) asymmetric $\Sigma 11$ tilt, (b) CuNb KS1, and (c) ARB KS interfaces. Blue particles represent vacancies while purple describes interstitial-like particles before the interaction. Green particles represent vacancies and red describes interstitial-like particles after the interaction. These are identified via a lattice-reference method in which the structure is compared before and after the reaction. In panel (a) gray atoms belong to unknown structure and black to hcp. In panels (b) and (c) gray and black atoms are Cu and Nb, respectively, belonging to the interface. The maps in the insets show the vacancy-interface interaction energy with the pristine interface.

the fact that the extended defect might saturate when trying to absorb a large collection of vacancies (and this does seem to be a factor, as seen for the 2° twist boundary). Further, the distribution of low-energy sites for vacancies at the extended defect may play a role in how the vacancies of the SFT are absorbed. However, the energetics of single vacancies does provide an indication of the propensity for the interface to absorb SFTs.

For the cases of heterophase interfaces, we observe a similar trend. The interaction energy for a single vacancy with both interfaces is highly attractive and in both cases the SFTs were fully absorbed (with some remnants at the PVD KS). In the case of the PVD KS interface, the thermodynamic force is lower and some delocalized debris is still distinguishable at the misfit dislocation intersections at the interface, possibly a consequence of the more distributed nature of the MDIs and the low-energy sites for vacancies. On the other hand, in the case of the ARB KS interface, which exhibits a stronger interaction with monovacancies, the SFT becomes fully absorbed. These results support the hypothesis of a direct correlation between the single-vacancy interaction energy and the capacity of the boundary to absorb SFTs.

While the maximum atomic volume at the interface does not seem to correlate directly with the SFT-interface interaction (see Table II), the minimum atomic volume shows a direct trend. The sites at the interface with minimum atomic volume are usually under compression and therefore the vacancy tends to sit on those sites since it reduces the elastic energy. The variation in the elastic energy is part of the total interaction energy, and therefore, there is a relation between the atomic volume and the vacancy interaction energy. Our results show that as the minimum atomic volume decreases the propensity of SFT absorption at the interface increases. This is the case for the dislocations and both homophase and heterophase interfaces.

It is important to note that the fact that the interface properties might be negligibly affected by the interaction with the SFT will have consequences in the long-term behavior of the system, as the sink properties of the extended defect will persist for a longer period of time. For the surfaces and interfaces in which the SFT is fully absorbed, the sink efficiency (defined as the flux of defects toward the interface relative to the flux of defects to an ideal sink) is close to one. We have not studied the saturation properties of the extended defects as SFTs accumulate, but we hypothesize that an easy absorption leads to better sink efficiencies, and likely, these better sink efficiencies will last further in time. Further, in an irradiation context, features such as dislocations, grain boundaries, and heterophase interfaces have been shown to preferentially absorb interstitials during collision cascades [41,51] and the resulting damaged state of these features leads to stronger interactions with single vacancies. This suggests that the interaction of SFTs with, for example, interfaces will be even stronger than indicated in the present simulations and that, especially during irradiation, the combined interaction of SFTs and damaged (interstitial loaded) interfaces will lead to enhanced recombination of radiation-induced defects than if these interactions were not present.

To obtain a deeper understanding of the structural reconfiguration of the combined SFT-interface system, we have analyzed the atomic displacements related to the configuration prior to the interaction in three cases: the asymmetric $\Sigma 11$ tilt, PVD KS, and ARB KS interfaces. The results are presented in Fig. 11 with blue and purple atoms representing vacancies and interstitial atoms before the reaction and green and red particles characterizing vacancies and interstitials after the interaction. (Note that in this lattice-reference scheme, an SFT is represented by a collection of vacancies and interstitials.) For the asymmetric $\Sigma 11$ tilt grain boundary, the gray and black atoms are in unknown and hcp structures, respectively, according to a common neighbor analysis [30], and we note that the extra vacancies transported by the SFT to the interface align along the Shockley partial dislocation lines. In the heterophase cases, gray and black atoms represent Cu and Nb, respectively, at the interface. For the PVD KS interface, the extra vacancies are distributed among contiguous MDIs. On the other hand, in the case of the ARB KS, the extra vacancies are fully delocalized, distributing across the interface, and also becoming aligned with the misfit dislocation cores. This seems to be a consequence of the distribution of sites with lower vacancy formation energy, as shown in the insets. In the case of the PVD KS interface the sites are localized close to the MDIs. In turn, for the ARB KS and asymmetric $\Sigma 11$ interfaces, the sites are more aligned with the dislocation cores. Therefore, the final microstructure seems to be related to the sites where the vacancy formation energy is lower.

Finally, to comprehend the implications of the mobility of SFTs and their possible absorption at different interfaces on larger scale observables, we have simulated the evolution of a system under irradiation at a dose rate of $5.5\ 10^{-4}$ dpa/s at 700 K for 1 s using an object kinetic Monte Carlo (OKMC) approach as implemented in MMONCA [52]. Our simulation box has dimensions of $50 \times 50 \times 200$ nm with absorbing boundary conditions in the z direction and periodic in the other two, mimicking the presence of interfaces with the capacity of fully absorbing the SFTs. We suppose that the self-interstitials immediately disappear at the sinks and we have not explicitly simulated them. We have calculated the diffusivities for vacancy clusters up to a size of nine at 700 K using MD, with the values shown in Table III. It is worth noting the large vacancy binding energy of the pentavacancy cluster and its low mobility, probably due to its compact ground state configuration. This is in agreement with previous studies carried out in Al [53]. For the case where we have

TABLE III. Diffusion coefficient (D) at 700 K and single vacancy binding energy (E_{bind}) depending on the vacancy cluster size.

Cluster size	D ($\frac{\text{cm}^2}{\text{s}}$)	E_{bind} (eV)
1	$1.25\ 10^{-8}$	
2	$1.822\ 10^{-8}$	− 0.143
3	$8.056\ 10^{-8}$	− 0.286
4	$3.55\ 10^{-8}$	− 0.134
5	$1.561\ 10^{-10}$	− 0.439
6	$2.720\ 10^{-8}$	− 0.288
7	$2.218\ 10^{-8}$	− 0.136
8	$1.345\ 10^{-8}$	− 0.433
9	$1.867\ 10^{-9}$	− 0.444

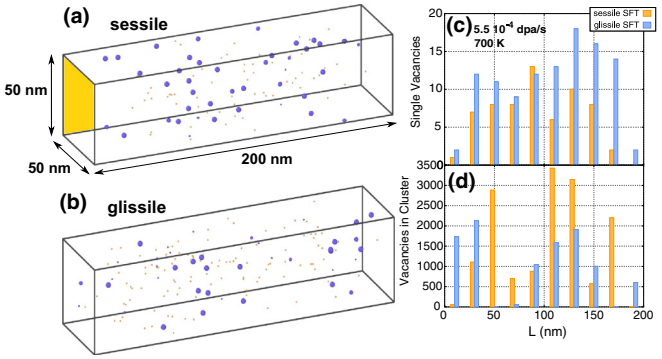

FIG. 12. Single vacancies (brown) and vacancy clusters (blue) found from OKMC simulations considering vacancy clusters (SFTs) as (a) sessile or (b) glissile at 700 K and a dose rate of 5.5 10^{-4} dpa/s after 1 s. Panel (c) shows the distribution of single vacancies and panel (d) shows the distribution of vacancies in clusters for both cases. L denotes the dimension perpendicular to the interfaces.

considered SFTs as mobile entities we have set the mobilities to $D^{D}_{\mathrm{SFT}} = 8.110^{-8}\exp(-0.092s)$, as obtained in Ref. [20], where s is the size of the SFT (in terms of the number of vacancies). For the sessile case, vacancy clusters larger than four were considered immobile, as has been traditionally done in the literature [54]. We have calculated the binding energies of single vacancies to vacancy clusters up to a size of nine. For larger clusters, we have taken the binding energy laws from the literature (Ref. [54]) such that we consider vacancy emission effects. While some of the assumptions behind these choices in parameters are not fully justified, the main goal of the OKMC simulations is to study the global implications of glissile SFTs on mesoscopic observables and therefore the used parameters should be sufficient for that purpose. Figure 12 shows the main results of the simulations. We observe that in the case where the SFTs are considered mobile, the amount of clusters larger than ten vacancies in the system is lower compared to the case in which the SFTs are immobile. For the mobile case we found 24 clusters larger than ten vacancies versus 33 in the immobile case, with an average cluster size of 418.42 and 447.21 vacancies per cluster, respectively. Large clusters are less likely to form when small and intermediate-sized SFTs are able to diffuse since they may reach the interface, where they are annihilated. In contrast, if the SFTs are immobile, they are not able to escape to sinks and will thus act as sinks themselves for smaller vacancy clusters and, consequently, grow. This implies that a larger denuded zone, especially for larger clusters, will be found in the case of mobile defects.

V. CONCLUSIONS

In summary, we have analyzed the interaction of mobile SFTs with different types of extended defects: free surfaces, dislocations, and interfaces in single phase Cu and Cu-Nb nanolaminates. The mobility of the small-to-intermediate-sized SFTs allows for the possibility of their diffusion towards sinks. We have shown how the probability of absorption of SFTs at the studied extended defects correlates with the single-vacancy interaction energy: As the interaction is more attractive, the complete absorption of the cluster becomes more probable. This easy-to-calculate quantity depends strongly on the atomic structure of these extended defects, which suggests the possibility of tailoring the atomic structure to improve the sink properties of the material. We have also examined the mesoscopic implications of the SFT mobility and annihilation of the SFTs at planar sinks via object kinetic Monte Carlo simulations. We have observed that the defect distribution differs substantially when considering these defects as mobile versus sessile entities and that the cluster sizes are larger when defects are immobile, which has implications in mesoscopic observables like void denuded zones, with a larger width in the cases where the defects can migrate.

ACKNOWLEDGMENTS

The authors gratefully acknowledge the support of the US Department of Energy (DOE) through the LANL/LDRD Program for this work. This research used resources provided by the LANL Institutional Computing Program. LANL, an affirmative action/equal opportunity employer, is operated by Los Alamos National Security, LLC, for the National Nuclear Security Administration of the US DOE under Contract No. DE-AC52-06NA25396.

[1] J. W. Wang, S. Narayanan, J. Y. Huang, Z. Zhang, T. Zhu, and S. X. Mao, Atomic-scale dynamic process of deformation-induced stacking fault tetrahedra in gold nanocrystals, Nat. Commun. **4**, 2340 (2013).

[2] H. Wang, D. Xu, R. Yang, and P. Veyssière, The formation of stacking fault tetrahedra in Al and Cu I dipole annihilation and the nucleation stage, Acta Mater. **59**, 1 (2011).

[3] M. J. Makin and F. J. Minter, Irradiation hardening in copper and nickel, Acta Mater. **8**, 691 (1960).

[4] Y. Matsukawa, Y. N. Osetsky, R. E. Stoller, and S. J. Zinkle, Mechanisms of stacking fault tetrahedra destruction by gliding dislocations in quenched gold, Philos. Mag. **88**, 581 (2008).

[5] R. Schibli and R. Schäublin, On the formation of stacking fault tetrahedra in irradiated austenitic stainless steels—a literature review, J. Nucl. Mater. **442**, S761 (2013).

[6] J. Robach, I. Robertson, H.-J. Lee, and B. Wirth, Dynamic observations and atomistic simulations of dislocation-defect interactions in rapidly quenched copper and gold, Acta Mater. **54**, 1679 (2006).

[7] Y. N. Osetsky, R. E. Stoller, D. Rodney, and D. J. Bacon, Atomic-scale details of dislocation–stacking fault tetrahedra interaction, Mater. Sci. Eng. A **400**, 370 (2005).

[8] E. Martinez, J. Marian, A. Arsenlis, M. Victoria, and J. M. Perlado, A dislocation dynamics study of the strength of stacking fault tetrahedra, part i: interactions with screw dislocations, Philos. Mag. **88**, 809 (2008).

[9] E. Martinez, J. Marian, and J. M. Perlado, A dislocation dynamics study of the strength of stacking fault tetrahedra, part ii: interactions with mixed and edge dislocations, Philos. Mag. **88**, 841 (2008).

[10] J. Marian, E. Martinez, H.-J. Lee, and B. D. Wirth, Micro/meso-scale computational study of dislocation–stacking fault tetrahedron interactions in copper, J. Mater. Res. **24**, 3628 (2009).
[11] M. Kiritani, Story of stacking fault tetrahedra, Mater. Chem. Phys. **50**, 133 (1997).
[12] J. Silcox and P. B. Hirsch, Direct observations of defects in quenched gold, Philos. Mag. **4**, 72 (1959).
[13] H. Kimura, D. Kuhlmann-Wilsdorf, and R. Maddin, Thegrwoth mechanism of stacking-fault tetrahedra in quenched gold, Appl. Phys. Lett. **3**, 4 (1963).
[14] S. J. Zinkle, L. E. Seitzman, and W. G. Wolfer, Stability of vacancy clusters in metals: I. energy calculations for pure metals, Philos. Mag. A **55**, 111 (1987).
[15] Y. Matsukawa, K. Yasunaga, M. Komatsu, and M. Kiritani, Dynamic observation of dislocation-free plastic deformation in gold thin foils, Mater. Sci. Eng. A **350**, 17 (2003).
[16] R. Schäublin, Z. Yao, N. Baluc, and M. Victoria, Irradiation-induced stacking fault tetrahedra in fcc metals, Philos. Mag. A **85**, 769 (2005).
[17] B. P. Uberuaga, R. G. Hoagland, A. F. Voter, and S. M. Valone, Direct Transformation of Vacancy Voids to Stacking Fault Tetrahedra, Phys. Rev. Lett. **99**, 135501 (2007).
[18] J. P. Hirth and J. Lothe, *Theory of Dislocations*, 2nd ed. (Krieger, Malabar, Florida, 1982).
[19] M. J. Sabochick and S. Yip, Migration energy calculations for small vacancy clusters in copper, J. Phys. F **18**, 1689 (1988).
[20] E. Martinez and B. P. Uberuaga, Mobility and coalescence of stacking fault tetrahedra in Cu, Sci. Rep. **5**, 9084 (2015).
[21] L. A. Zepeda-Ruiz, E. Martinez, M. Caro, E. G. Fu, and A. Caro, Deformation mechanisms of irradiated metallic nanofoams, Appl. Phys. Lett. **103**, 031909 (2013).
[22] M. Caro, W. M. Mook, E. G. Fu, Y. Q. Wang, C. Sheehan, E. Martinez, J. K. Baldwin, and A. Caro, Radiation-induced effects on mechanical properties of nanoporous gold foams, Appl. Phys. Lett. **104**, 233109 (2014).
[23] W. Z. Han, M. J. Demkowicz, E. G. Fu, Y. Q. Wang, and A. Misra, Effect of grain boundary character on sink efficiency, Acta Mater. **60**, 6341 (2012).
[24] W. Z. Han, M. J. Demkowicz, N. A. Mara, E. G. Fu, S. Sinha, A. D. Rollet, Y. Q. Wang, J. S. Carpenter, I. J. Beyerlein, and A. Misra, Design of radiation tolerant materials via interface engineering, Adv. Mater. **25**, 6975 (2013).
[25] N. A. Mara and I. J. Beyerlein, Review: effect of bimetal interface structure on the mechanical behavior of Cu-Nb fcc-bcc nanolayered composites, J. Mater. Sci. **49**, 6497 (2014).
[26] X.-M. Bai, L. Vernon, R. G. Hoagland, A. F. Voter, M. Nastasi, and B. P. Uberuaga, Role of atomic structure on grain boundary-defect interactions in Cu, Phys. Rev. B **85**, 214103 (2012).
[27] S. Plimpton, Fast parallel algorithms for short-range molecular dynamics, J. Comput. Phys. **117**, 1 (1995).
[28] Y. Mishin, M. J. Mehl, D. A. Papaconstantopoulos, and A. F. Voter, Structural stability and lattice defects in copper: Ab initio, tight-binding, and embedded-atom calculations, Phys. Rev. B **63**, 224106 (2001).
[29] L. Zhang, E. Martinez, A. Caro, X.-Y. Liu, and M. J. Demkowicz, Liquid-phase thermodynamics and structures in the Cu-Nb binary system, Modell. Simul. Mater. Sci. Eng. **21**, 025005 (2013).
[30] A. Stukowski, Visualization and analysis of atomistic simulation data with OVITO, the open visualization tool, Modell. Simul. Mater. Sci. Eng. **18**, 015012 (2010).
[31] A. Stukowski, Structure identification methods for atomistic simulations of crystalline materials, Modell. Simul. Mater. Sci. Eng. **20**, 045021 (2012).
[32] B. D. Wirth, V. V. Bulatov, and T. Diaz de la Rubia, Dislocation-stacking fault tetrahedron interactions in Cu, J. Eng. Mater. Technol. Trans. ASME **124**, 329 (2002).
[33] D. Rodney, Atomic-scale modeling of clear band formation in FCC metals, Nucl. Instrum. Methods Phys. Res., Sect. B **228**, 100 (2005).
[34] P. Szelestey, M. Patriarca, and K. Kaski, Computational study of a screw dislocation interacting with a stacking-fault tetrahedron, Modell. Simul. Mater. Sci. Eng. **13**, 541 (2005).
[35] Y. N. Osetsky, Y. Matsukawa, R. E. Stoler, and S. J. Zinkle, On the features of dislocation-obstacle interaction in thin films: large-scale atomistic simulation, Philos. Mag. Lett. **86**, 511 (2006).
[36] H. J. Lee, J. H. Shim, and B. D. Wirth, Molecular dynamics simulation of screw dislocation interaction with stacking fault tetrahedron in face-centered cubic Cu, J. Mater. Res. **22**, 2758 (2007).
[37] H. Wang, D. Xu, R. Yang, and P. Veyssiere, The formation of stacking fault tetrahedra in Al and Cu II: sft growth by successive absorption of vacancies generated by dipole annihilation, Acta Mater. **59**, 10 (2011).
[38] H. Wang, D. Xu, R. Yang, and P. Veyssiere, The formation of stacking fault tetrahedra in Al and Cu III: growth by expanding ledges, Acta Mater. **59**, 19 (2011).
[39] M. Niewczas, and R. G. Hoagland, Molecular dynamics studies of the interaction of $a/6\langle 112\rangle$ Shockley dislocations with stacking fault tetrahedra in copper, part i: intersection of SFT by an isolated Shockley, Philos. Mag. **89**, 623 (2009).
[40] M. Niewczas and R. G. Hoagland, Molecular dynamics studies of the interaction of $a/6\langle 112\rangle$ Shockley dislocations with stacking fault tetrahedra in copper, part ii: intersection of stacking fault tetrahedra by moving twin boundaries, Philos. Mag. **89**, 727 (2009).
[41] X.-M. Bai, A. F. Voter, R. G. Hoagland, M. Nastasi, and B. P. Uberuaga, Efficient annealing of radiation damage near grain boundaries via interstitial emission, Science **327**, 1631 (2010).
[42] E. Martínez, J. P. Hirth, M. Nastasi, and A. Caro, Structure of a 2° (010) Cu twist boundary interface and the segregation of vacancies and He atoms, Phys. Rev. B **85**, 060101(R) (2012).
[43] E. Martínez and A. Caro, Atomistic modeling of long-term evolution of twist boundaries under vacancy supersaturation, Phys. Rev. B **86**, 214109 (2012).
[44] E. Martínez, A. Caro, and I. J. Beyerlein, Atomistic modeling of defect-induced plasticity in Cu-Nb nanocomposites, Phys. Rev. B **90**, 054103 (2014).
[45] I. J. Beyerlein, J. Wang, and R. F. Zhang, Interface-dependent nucleation in nanostructured layered composites, Appl. Phys. Lett. Mater. **1**, 032112 (2013).
[46] R. F. Zhang, J. Wang, I. J. Beyerlein, A. Misra, and T. C. Germann, Atomic-scale study of nucleation of dislocations from fcc-bcc interfaces, Acta Mater. **60**, 2855 (2012).
[47] K. Kolluri and M. J. Demkowicz, Dislocation mechanism of interface point defect migration, Phys. Rev. B **82**, 193404 (2010).

[48] B. P. Uberuaga, L. J. Vernon, E. Martinez, and A. F. Voter, The relationship between grain boundary structure, defect mobility, and grain boundary sink efficiency, Sci. Rep. **5**, 9095, (2015).

[49] K. Yu, D. Bufford, C. Sun, Y. Liu, H. Wang, M. A. Kirk, M. Li, and X. Zhang, Removal of stacking-fault tetrahedra by twin boundaries in nanotwinned metals, Nat. Commun. **4**, 1377 (2013).

[50] J. Li, K. Y. Yu, Y. Chen, M. Song, H. Wang, M. A. Kirk, M. Li, and X. Zhang, In situ study of defect migration kinetics and self-healing of twin boundaries in heavy ion irradiated nanotwinned metals, Nano Lett. **15**, 2922 (2015).

[51] X.-Y. Liu, B. P. Uberuaga, M. J. Demkowicz, T. C. Germann, A. Misra, and M. Nastasi, Mechanism for recombination of radiation-induced point defects at interphase boundaries, Phys. Rev. B **85**, 012103 (2012).

[52] I. Martin-Bragado, A. Rivera, G. Valles, J. L. Gomez-Selles, and M. J. Caturla, MMONCA: an object kinetic Monte Carlo simulator for damage irradiation evolution and defect diffusion, Comput. Phys. Commun. **184**, 2703 (2013).

[53] H. Wang, D. Rodney, D. Xu, R. Yang, and P. Veyssiere, Pentavacancy as the key nucleus for vacancy clustering in aluminum, Phys. Rev. B **84**, 220103(R) (2011).

[54] M. J. Caturla, N. Soneda, E. Alonso, B. D. Wirth, T. D. de la Rubia, and J. M. Perlado, Comparative study of radiation damage accumulation in Cu and Fe, J. Nucl. Mater. **276**, 13 (2000).